Nano Energy 73 (2020) 104822

Contents lists available at ScienceDirect

Nano Energy

journal homepage: http://www.elsevier.com/locate/nanoen

Ultralow thermal conductivity and negative thermal expansion of CuSCN

Yupeng Shen, Fancy Qian Wang, Qian Wang *

Center for Applied Physics and Technology, Department of Materials Science and Engineering, HEDPS, BKL-MEMD, College of Engineering, Peking University, Beijing, 100871, China

ARTICLE INFO

Keywords:
Thermal conductivity
Thermal expansion
CuSCN
Density functional
Theory
Thermoelectric

ABSTRACT

Copper thiocyanate (CuSCN) has recently received considerable attention because of its high hole mobility and applications in solar cells [*Science* 358(2017)768]. In this work, by performing state-of-the-art theoretical calculations, for the first time we find that the thermal conductivities of both α- and β-CuSCN are ultralow with the values of 1.2 and 2.4 W/mK at room temperature, respectively. Based on detailed analyses of the phonon dispersion, Grüneisen parameters, three phonon scattering rates and atomic displacement parameters, we further demonstrate that the underlying reasons for the ultralow thermal conductivities are due to the avoided crossing between the longitudinal acoustic (LA) phonons and the low-lying optical branches as well as the weak bonding and strong anharmonicity. The low lattice thermal conductivities lead to high *ZT* values of 1.7 and 2.1 at 800 K for α- and β-CuSCN, respectively. In addition, both materials exhibit large negative thermal expansion (NTE) coefficients originated from the transverse vibrations in Cu–N–C–S chains. These features endow CuSCN with the potential for thermal barrier coating and thermal devices going beyond the reported photovoltaic applications.

1. Introduction

Materials with low thermal conductivity have a wide range of applications in thermal barrier coatings and thermoelectric devices. In turbine engines, thermal barrier coatings have a large impact on the cost and lifetime of the system [1]. Especially, the usage of thermal barrier coatings can improve Carnot efficiency [2]. Currently the most widely used coating material is yttria stabilized zirconia because of its low thermal conductivity (2.0–3.0 W/mK) [3,4] and good mechanical properties [5]. However, it has some shortcomings as well, such as limited phase stability induced by the conversion of metastable phases [6], and loss of capability owing to sintering at high temperature [7], which significantly affect the efficiency and mechanical strength. Therefore, it is highly desirable to find new thermal barrier coating materials with low thermal conductivity. While in thermoelectric devices, the parameter for measuring the performance is the figure of merit defined as $zT = S^2\sigma T/(\kappa_e+\kappa_L)$, in which S is the Seebeck coefficient, σ is the electric conductivity, T is the absolute temperature, and κ_L and κ_e are lattice thermal conductivity and electronic thermal conductivity, respectively. Owing to the strong coupling among the parameters S, κ_e and σ [8], using materials with low κ_L is an effective way to achieve high thermoelectric performance [9]. Therefore, finding materials with low thermal conductivity and exploring the physical mechanism are essential for making the progress in thermoelectric devices.

On the other hand, materials with low thermal conductivity usually possess the following features: (i) weak interatomic bonding, (ii) complicated geometry structure, (iii) strong anharmonicity, and (iv) large average atomic mass and high atomic mass contrast [10,11]. Therefore, copper thiocyanate (CuSCN) has the potential to possess low thermal conductivity because of the weak interatomic bonding and large atomic mass contrast. In addition, CuSCN has good chemical stability with cheap price [12], is benign to environment [13], and especially, is feasible to be prepared with high purity [14]. These features make CuSCN be widely used in perovskite solar cells (PSCs) [15], thin-film transistors (TFTs) [16], organic-light emitting diodes (OLEDs) [17], dye-sensitized solid-state solar cells (DSSCs) [18] and bulk-heterojunction (BHJ) organic solar cells [19]. However, the research on the thermal conductivity of CuSCN has not yet been seen, which motivates us to carry out this study on the thermal conductivity, thermoelectric performance and negative thermal expansion of CuSCN.

2. Computational methods

The calculations are based on density functional theory (DFT) and the projector augmented wave (PAW) method [20] within the Vienna Ab initio Simulation Package (VASP) [21]. The Perdew-Burke-Ernzerhof

* Corresponding author.
E-mail address: qianwang2@pku.edu.cn (Q. Wang).

https://doi.org/10.1016/j.nanoen.2020.104822
Received 16 December 2019; Received in revised form 22 March 2020; Accepted 8 April 2020
Available online 18 April 2020

(PBE) exchange-correlation functional for the generalized gradient approximation (GGA) [22] is used to treat the electronic exchange-correlation interaction. In geometry optimization, the convergence thresholds of total energy and force component are 10^{-6} eV and 10^{-4} eV/Å, respectively. The K points with a grid density of $2\pi \times 0.02$ Å^{-1} are employed to represent the Brillouin zone.

The thermal conductivities of the two structures are calculated by solving phonon Boltzmann transport equation (BTE) as implemented in the ShengBTE package [23]. To obtain the harmonic (second order) and anharmonic (third order) interatomic force constants (IFCs) of α- and β-CuSCN as the input files of calculations, a $3 \times 3 \times 2$ supercell for α phase and a $4 \times 4 \times 2$ supercell for β phase are constructed, and the corresponding IFCs are acquired by DFT calculations performed in VASP.

In order to simulate the thermal expansion of α- and β-CuSCN at different temperatures, we adopt the self-consistent quasiharmonic approximation (SCQHA) method [24], which has been successfully applied in many systems, such as $SrTiO_3$ [25] and $Ca_3Ti_2O_7$ [26]. Compared with the conventional quasiharmonic approximation method [27–29], the SCQHA method requires less phonon calculations and shows better accuracy [24]. And the volume thermal-expansion coefficient (α) is calculated by using the relation of $\alpha = \frac{1}{V}\frac{dV}{dT}$.

3. Results and discussion

3.1. Geometry and stability

CuSCN possesses two stable different geometric configurations [30], α- and β-phase, as shown in Fig. 1a and b. With the Cu–N–C–S atom chain as the building block, the orthorhombic α-CuSCN unit cell can be obtained by rotation of the building blocks and bonding between Cu and S atoms, while the hexagonal β-CuSCN can be obtained by translation of the building blocks and connection between Cu and S atoms. The space group of α-CuSCN is *Pbca* (61) and the lattice constants are $a = 7.27$ Å, $b = 6.71$ Å, and $c = 10.94$ Å. There are 32 atoms in the unit cell of α-CuSCN. For β-CuSCN containing 8 atoms in a unit cell, it has the space group *P63mc* (186), and the lattice parameters are $a = b = 3.85$ Å, and $c = 10.94$ Å. These lattice parameters are in good agreement with previous work [30,31]. For the two phases, β-CuSCN is energetically more favorable [30]. Both phases are p-type semiconductors with a band gap of about 3.6 eV [14,32], and can be prepared from the solution in different preparation processes [32].

First, we calculate the phonon dispersion of α- and β-CuSCN, and plot the results in Fig. 2a and b, where the three acoustic branches (TA, TA' and LA) and optical phonon branches are distinguished by different colors. One can see that in the entire Brillouin zones of the two structures, there are no any negative frequencies, suggesting that the two phases are dynamically stable. It is worth noting that the phonon dispersions of both α- and β-CuSCN display avoided crossing between the longitudinal acoustic (LA) phonons and low lying optical (LLO) branches. As shown in the red circles in Fig. 2c–f, the avoided crossing occurs in the Γ-X, Y-Γ and Γ-Z high-symmetry paths in α-CuSCN, and the K-Γ in β-CuSCN. Such feature has also been found in PbTe [33] and $Ba_8Ga_{16}Ge_{30}$ [34], and is usually considered as one of the indicators of low thermal conductivity. The avoided crossing represents the strong coupling between phonons, and the width of the gap of the avoided crossing indicates the strength of the coupling [35]. In general, the avoided crossing can reduce thermal conductivity in three ways. Firstly, the avoided crossing between the LA phonons and optical phonons would result in an abnormal damping and lowering the LA phonons, and thus leading to low group velocity of the LA phonons [33]. The decrease of LA phonon group velocity reduces the thermal conductivity. Secondly, the avoided crossing can increase the scattering rates of the LA phonons and decreases the phonon lifetimes [34], thus leading to low thermal conductivity [35,36]. Thirdly, the avoided crossing can soften the LA branches, resulting in low Debye temperature θ_D [37], which is one of the indicators of low thermal conductivity [38]. As shown in the phonon dispersion figures of α-CuSCN, the coupling between the LA and LLO branches in the Γ-Z direction is much stronger than that in the Γ-X and Γ-Y directions. Moreover, the coupling strength in α-CuSCN is stronger than that in β-CuSCN, indicating that α-CuSCN may possess lower thermal conductivity as compared with that of β-CuSCN.

3.2. Ultralow thermal conductivity and mechanism

Next, we calculate the lattice thermal conductivity (κ_L) to characterize the performance of heat transport. The intrinsic κ_L of α- and β-CuSCN as a function of temperature is plotted in Fig. 3a. At room temperature (300 K), the thermal conductivities of α-CuSCN are 1.2, 1.2 and 1.5 W/mK in the x, y and z directions, respectively, and the thermal conductivities of β-CuSCN are 2.4 and 3.9 W/mK in the in-plane and out-of-plane directions, indicating that both α and β phases of CuSCN possess ultralow thermal conductivities, and the former has lower values than the latter as expected from the mechanism analysis discussed above. We further study the phonon group velocity and show the results in Fig. 3. In β-CuSCN, the phonon group velocity along the out-of-plane direction (Fig. 3c) is higher than that along the in-plane direction (Fig. 3b), which contributes to the larger thermal conductivity in out-of-plane direction. Similarly, in α-CuSCN, the phonon group velocity along the z direction (Fig. 3f) is slightly higher than that along the x and y directions (Fig. 3d

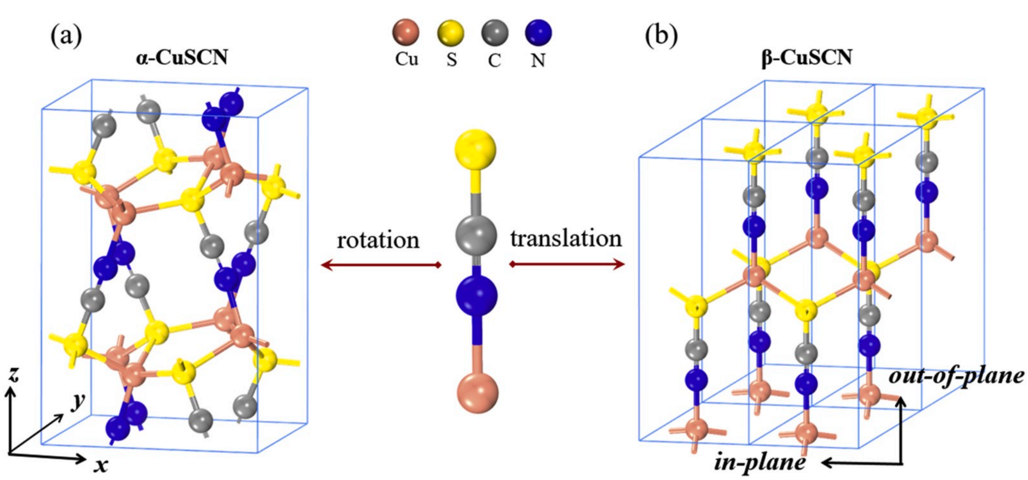

Fig. 1. Structure configuration of (a) α-CuSCN and (b) β-CuSCN. To better illustrate the two structures, the structural unit and the corresponding construction methods are also shown.

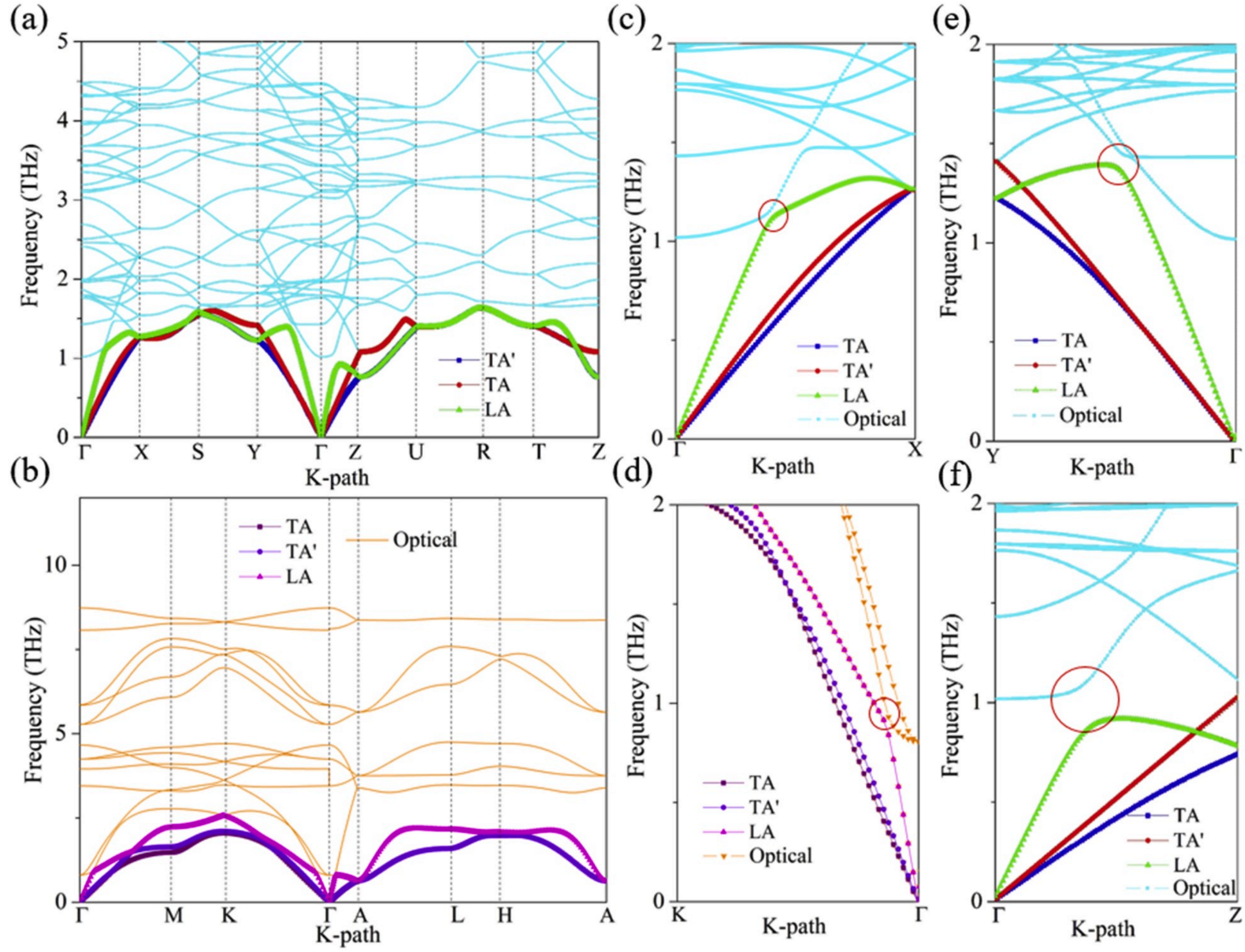

Fig. 2. Phonon dispersion of (a) α- and (b) β-CuSCN. Three acoustic phonon branches (TA, TA′ and LA) and optical branches are distinguished by different colors. Phonon dispersion for α-CuSCN in the low frequency region (0–2 THz) along the (c) Γ-X, (e) Y-Γ and (f) Γ-Z. (d) Phonon dispersion for β-CuSCN in the low frequency region (0–2 THz) along the K-Γ. The avoided crossing is marked in red circles.

and e), and the phonon group velocities along the x and y directions share similar feature of distribution, thus resulting in larger thermal conductivity in the z direction and similar thermal conductivities in the x and y directions.

Then, we analyze the bonding strength of the two structures. Since bonding strength is related to elastic parameters, we calculate the Young's modulus (E), Shear modulus (G) and Poisson ratio (ν_p) of the two structures by using the energy-strain method implemented in AELAS code [39]. The results are listed in Table 1. The elastic properties of some other materials with low thermal conductivity are also listed in the table for comparison. One can see that both α- and β-CuSCN have low Young's modulus and shear modulus. Generally, materials with low Young's modulus and shear modulus possess "soft bonding" feature, which would slow down phonon transport, resulting in low thermal conductivity [40].

To better understand the origin of low thermal conductivity, we analyze the three phonon scattering rates and weighted phase space of α- and β-CuSCN. The three-phonon scattering rates are related to the intensity of phonon scattering during heat conduction. If a material possesses high scattering rates, it means that the phonon scattering is strong, implying a low thermal conductivity. One can see that in Fig. 4a, both α-CuSCN and β-CuSCN exhibit high three-phonon scattering rates. We then calculate the three phonon phase space P_3 of the two structures, which characterizes the number of scattering channels for the phonons. When the other factors are the same, the larger P_3 that the material possesses, the higher resistance that phonon experiences in the transport process. As shown in Fig. 4b, the values of the three-phonon phase space of the two structures are relatively large, indicating that both structures would have low thermal conductivities. Moreover, both the scattering rates and the phase space of α-CuSCN are larger than those of the β phase, leading to a lower thermal conductivity of α-CuSCN, as compared to that of β-CuSCN.

To quantitatively measure the anharmonicity of the two structures, we calculate the mode Grüneisen parameters (γ) of the three acoustic modes and atomic displacement parameters (ADP) in α- and β-CuSCN. γ is defined as $\gamma = \frac{A}{\omega_\lambda} \frac{\partial \omega_\lambda}{\partial A}$, here A and ω_λ are the volume of the unit cell and angular frequency, respectively. Large Grüneisen parameter indicates strong anharmonicity of the structure, resulting in low thermal conductivity [46]. As one can see in Fig. 5a and b, α- and β-CuSCN share similar features with large Grüneisen parameters. For the convenience of comparison, we calculate the average Grüneisen parameters of α- and β-CuSCN. The corresponding results are 1.96 and 2.12, respectively, which are larger than those of many other materials with low thermal conductivity such as PbTe (1.65) [42], PbSe (1.69) [42] and $IrSb_3$ (1.42) [47], indicating strong anharmonicity in both α- and β-CuSCN.

In addition to Grüneisen parameter, anharmonicity is also related to the atomic displacement parameter (ADP) that measures the mean-square displacement of an atom around its equilibrium position. A large ADP value characterizes a weak bonding and large vibration, implying strong anharmonicity [48]. As shown in Fig. 5c, for α-CuSCN, N_x and Cu_y possess large ADP (0.032 Å^2 for N along the x direction and 0.029 Å^2 for Cu along the y direction at 300 K), indicating that N and Cu

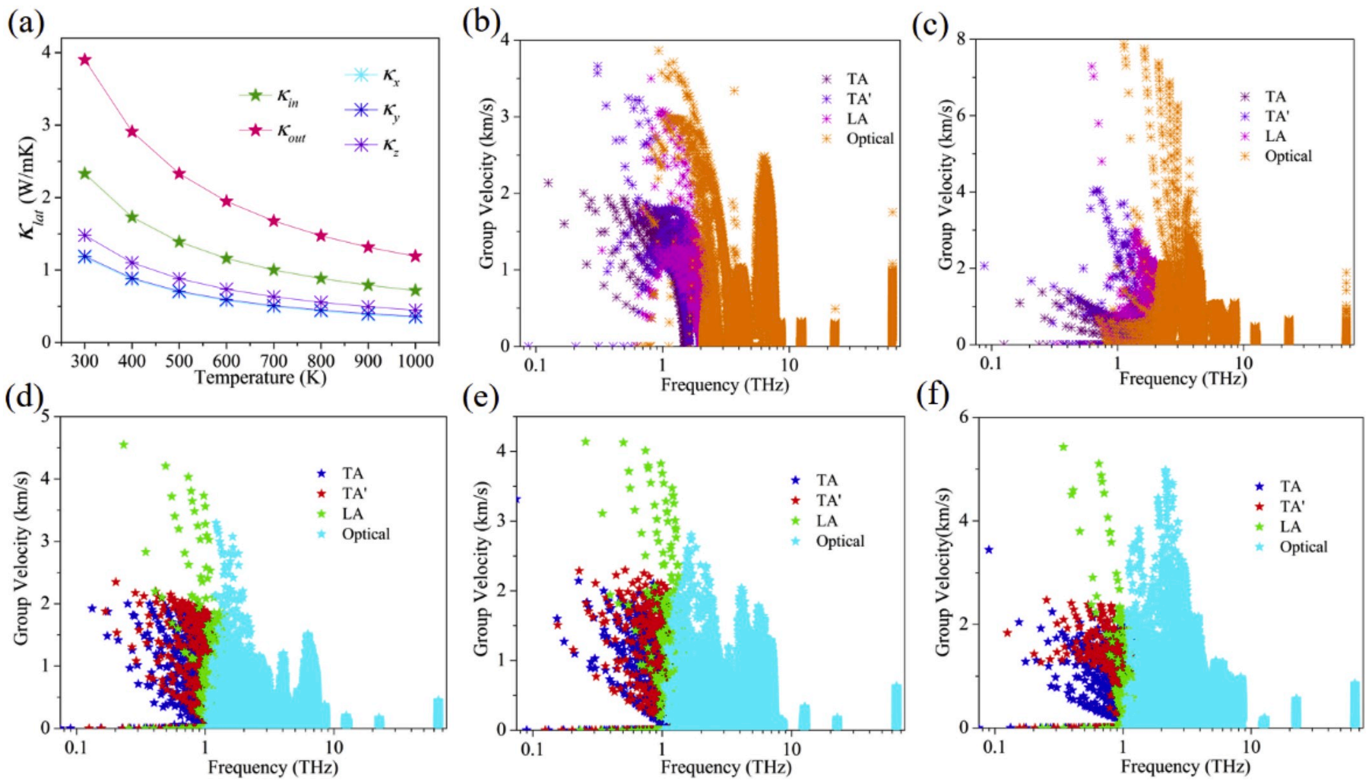

Fig. 3. (a) Lattice thermal conductivity as a function of temperature for α-CuSCN in the x, y, z directions (κ_x, κ_y, κ_z) and β-CuSCN in the in-plane and out-of-plane directions (κ_{in} and κ_{out}). Group velocity of β-CuSCN in the (b) in-plane and (c) out-of-plane direction, and group velocity of α-CuSCN in the (d) x direction, (e) y direction and (f) z direction. Three acoustic (TA, TA′ and LA) and optical phonon branches are distinguished by different colors.

Table 1
Calculated Young's modulus E (in GPa), shear modulus G (in GPa), Poisson's ratio v_p, thermal conductivity κ_L (in W/mK) and figure of merit ZT of α- and β-CuSCN. For comparison, the results of BiCuSeO, PbTe, SnSe and PbS are also given.

	E	G	v_p	κ_L	ZT
α-CuSCN	43.6	16.4	0.33	1.2	1.7
β-CuSCN	43.7	16.2	0.35	2.4	2.1
BiCuSeO	76.5 [41]	30.6 [41]	0.25 [41]	0.6 [41]	1.3 [41]
PbTe	53.7 [42]	21.2 [42]	0.26 [42]	2.3 [42]	2.2 [43]
SnSe	40.5 [42]	14.5 [42]	0.37 [42]	0.6 [42]	2.6 [44]
PbS	69.7 [42]	27.2 [42]	0.28 [42]	2.8 [42]	0.8 [45]

atoms are weakly bounded in a flat potential well along the x direction and the y direction, respectively. The similar situation also occurs in the N atoms and Cu atoms along the in-plane direction in β-CuSCN (0.033 Å^2 for N and 0.028 Å^2 for Cu along the in-plane direction at 300 K), which is plotted in Fig. 5d. The ADP values of α- and β-CuSCN are larger than the values of many other materials with low thermal conductivity, such as $CuSbS_2$ (0.015 Å^2) [49] and ZnSb (0.024 Å^2) [50]. The large Grüneisen parameters and ADP values of the two structures indicate the features of weak chemical bonding and strong anharmonicity, which lead to ultralow thermal conductivity.

3.3. Thermoelectric properties

Since both α- and β-CuSCN possess ultralow thermal conductivity, we then explore their potential for thermoelectric applications. The thermoelectric properties are calculated by using BoltzTrap2 program within the electron relaxation time (τ) approximation method [51], which has been widely used in previous studies [52,53]. We select three different temperatures (300, 600 and 800 K) to investigate the temperature dependence of thermoelectric properties and calculate the Seebeck coefficient (S), electrical conductivity (σ), and power factor (PF) defined as $PF = S^2\sigma$. For α-CuSCN along the x, y and z directions and β-CuSCN along the in-plane and out-of-plane directions, the results are plotted in Figs. S1 and S2, respectively. The peak values of S for α- and β-CuSCN at 300, 600 and 800 K are 1.6, 1.6, 1.5 mV/K and 1.6, 1.6, 1.3 mV/K, respectively, which are larger than those of PbTe [43] (0.4 mV/K at 300 K and 0.48 mV/K at 600 K) and SnSe [44] (0.53 mV/K at 300 K, 0.56 mV/K at 600 K and 0.40 mV/K at 800 K), implying that both α- and β-CuSCN are likely to have large figure of merit (ZT) values.

Different from the Seebeck coefficients, we find that the electrical conductivities of α- and β-CuSCN show anisotropy. For α-CuSCN, the values of electrical conductivities along the y and z directions are larger than that along the x direction. While for β-CuSCN, the electrical conductivity along the out-of-plane direction is larger than that along the in-plane direction. Based on Seebeck coefficient and electrical conductivity, we further calculate the power factor (PF) using the formula of $PF = S^2\sigma$. The results are plotted in Fig. S1g-i and S2e, f. When the power factor peaks, the chemical potential is different from that at which the Seebeck coefficient and electrical conductivity reach their maximums, suggesting that a suitable carrier concentration is of great significance for good thermoelectric performance.

We then calculate the ZT values by using the formula of $ZT = S^2\sigma T/\kappa_e{+}\kappa_L$. Here κ_e can be obtained by $\kappa_e = L\sigma T$, and L is the Lorenz number. The calculated results for α- and β-CuSCN at different temperatures are displayed in Fig. 6. For α-CuSCN, the ZT reaches the maximum in the y direction, which is 0.2, 1.0 and 1.7 at 300, 600 and 800 K, respectively. While for β-CuSCN, the ZT along the out-of-plane direction is higher than that along the in-plane direction with the value of 0.2, 1.2 and 2.1 at 300, 600 and 800 K, respectively. These values are comparable to those of some well-known thermoelectric materials including PbTe [43] (0.7 at 300 K and 2.2 at 600 K) and SnSe [44] (0.2 at 300 K, 0.3 at 600 K and 2.0 at 800 K), showing good potential for thermoelectric

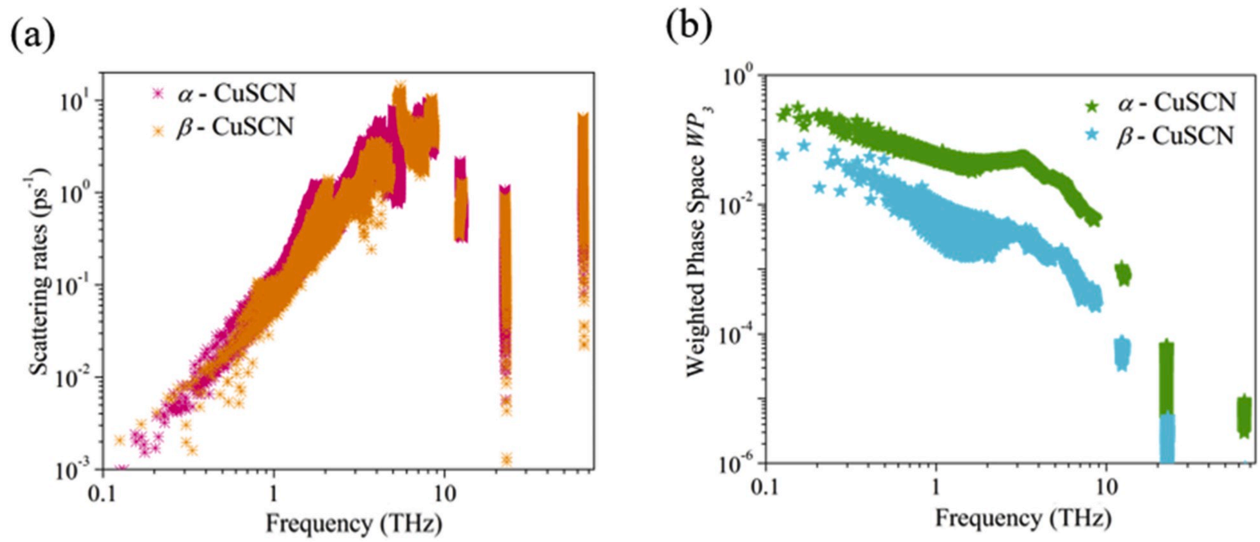

Fig. 4. (a) Three phonon scattering rates, and (b) weighted phase space of α- and β-CuSCN.

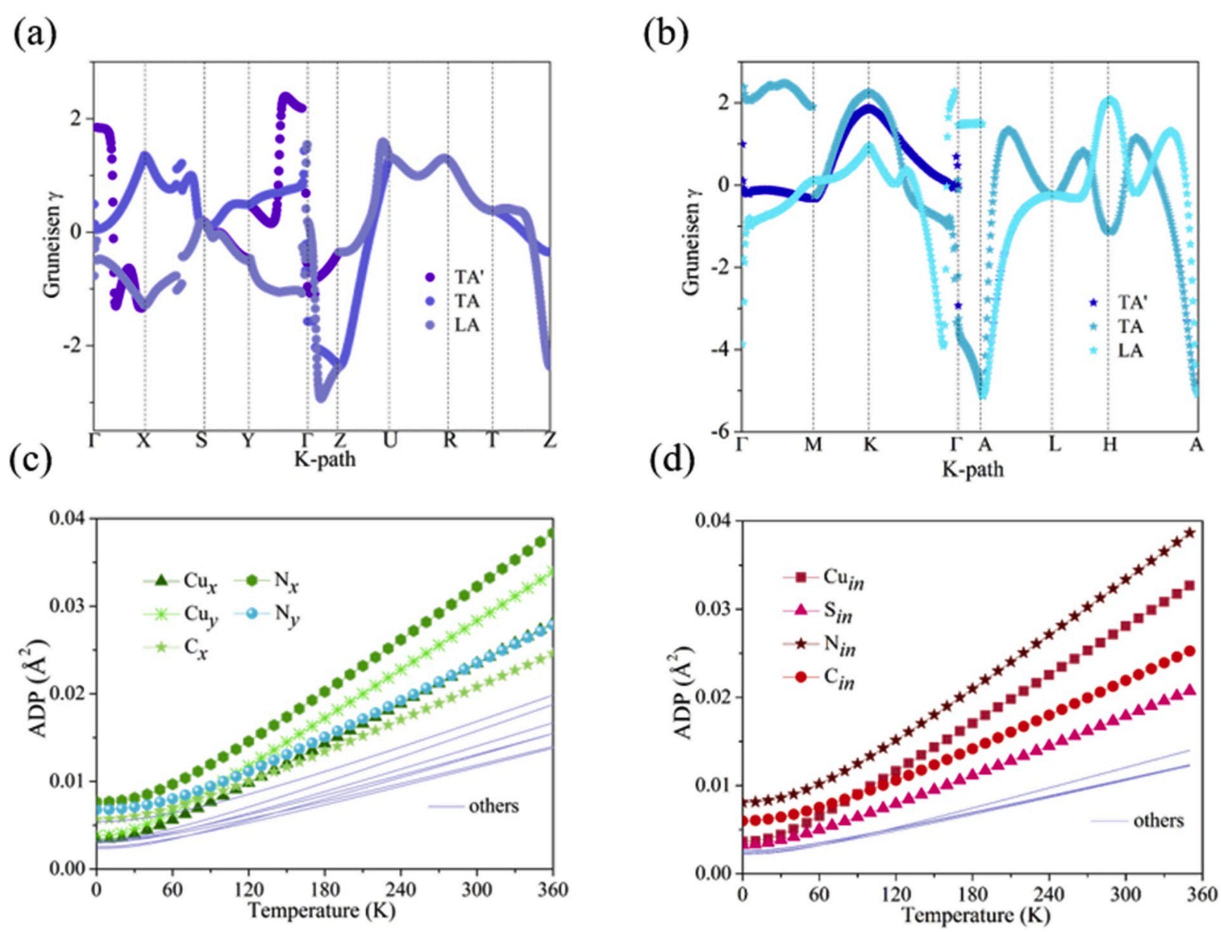

Fig. 5. Gruneisen parameters of (a) α- and (b) β-CuSCN. Calculated ADPs for different atoms with respect to temperature for (c) α- and (d) β-CuSCN.

applications.

3.4. Negative thermal expansion (NTE)

The coefficient of thermal expansion is also a key factor for measuring the thermal performance of a material at different temperatures. Generally, materials expand with increasing temperature, showing positive thermal expansion. However, the thermal expansion of materials would degrade the performance. Currently the most effective way to solve this problem is to obtain zero thermal expansion composites by combining positive thermal expansion material with negative thermal expansion material [54]. Therefore, it is important to find new materials with negative thermal expansion coefficient over a wide temperature range. We calculate the volume changes and coefficients of

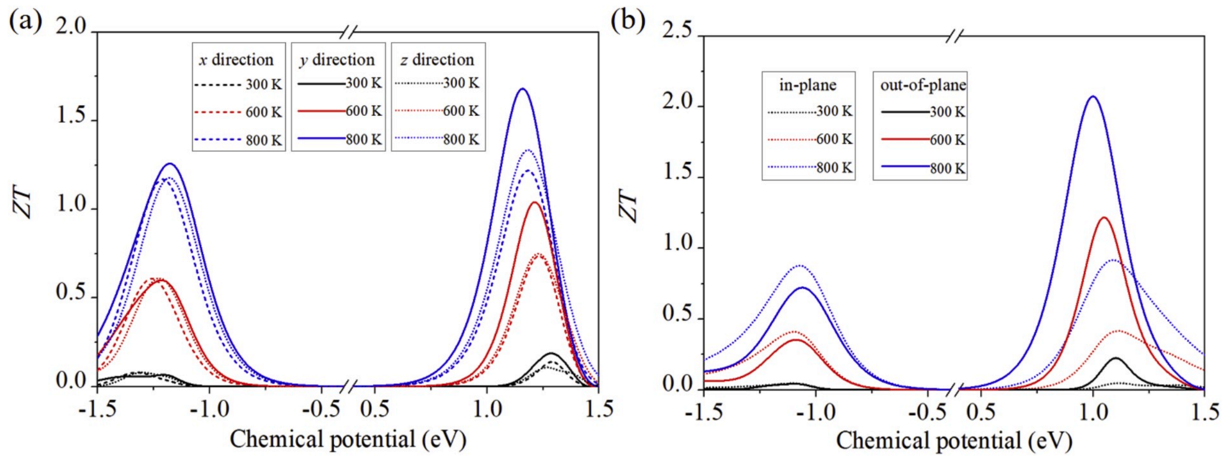

Fig. 6. Calculated figure of merit (*ZT*) as a function of chemical potential at the three different temperatures of (a) α-CuSCN along the *x*, *y* and *z* directions and (b) β-CuSCN along the in-plane and out-of-plane directions.

thermal expansion with respect to temperature for both α- and β-CuSCN using the SCQHA method [24]. The results are plotted in Fig. 7a and b, indicating that as temperature increases, the volumes of both structures gradually shrink, implying the feature of negative thermal expansion in these two structures.

The NTE properties of α- and β-CuSCN are mainly attributed to the transverse vibrations in the structures as suggested in previous studies of ZrW_2O_8 [55], ScF_3 [56] and SiO_2 zeolites [57], where the systems share a similar structural feature, namely two metal atoms are connected by a bridge atom, then forming a network [58]. The transverse vibrations can be seen from the ADP of α- and β-CuSCN, as shown in Fig. 5c and d, characterizing the intensity of vibration. For α-CuSCN, the vibration of *N* atoms along the *x* direction is the strongest (N_x), followed by Cu_y, N_y, Cu_x and C_x. It is worth noting that these strong vibrations are all along the transverse direction of Cu–N–C–S atom chains. A similar situation occurs in β-CuSCN. The strongest vibration in β-CuSCN is from *N* atoms along

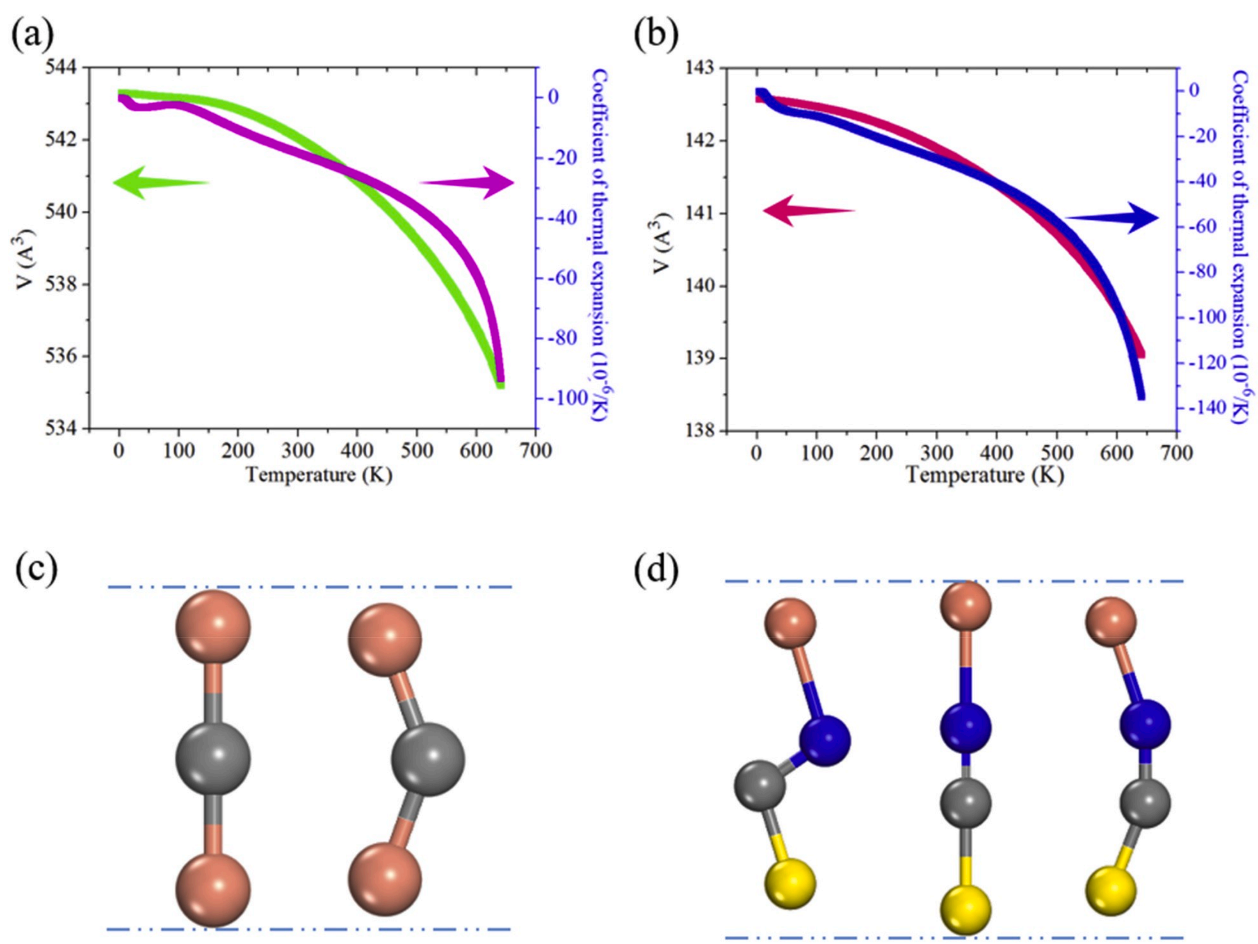

Fig. 7. Variations of volume and coefficient of thermal expansion with temperature of (a) α- and (b) β-CuSCN. Schematics of the transverse vibration models for (c) the single-atom and (d) the diatomic linkages.

the in-plane direction (N_{in}), and followed by Cu_{in}, C_{in} and S_{in}. These strong vibrations are also along the transverse direction of Cu–N–C–S atom chains. As shown in Fig. 7c, when temperature rises, the central bridge atoms will vibrate in the direction perpendicular to the chain axis, making the distance between the atoms at both ends shorter, thus exhibiting a macroscopic NTE feature [59]. In both α- and β-CuSCN, there are two bridge atoms (C and N) between Cu atom and S atom. As plotted in Fig. 7d, the C atom and N atom can vibrate in same or different directions, leading to NTE. And the larger degree of freedom would lead to stronger shrinkage in geometry. One can see from Fig. 7a and b that the coefficients of thermal expansion of α- and β-CuSCN at 300 K are about -20×10^{-6} K^{-1} and -30 $\times$ 10^{-6} K^{-1}, respectively, much significant as compared to the reported systems including ZrW_2O_8 (-8.8×10^{-6} K^{-1}) [55], ScF_3 (-7.5×10^{-6} K^{-1}) [56] and SiO_2 zeolites (-3.7×10^{-6} K^{-1}) [57]. Besides, the CuSCN units in β-CuSCN are more orderly arranged as compared to the case in α-CuSCN, which makes it more sensitive to transverse vibration, thus leading to stronger NTE.

4. Conclusions

Based on first-principles calculations and Boltzmann transport theory, we have found that both α- and β-CuSCN possess ultralow thermal conductivities of 1.2 and 2.4 W/mK at room temperature, respectively, which are lower than the reported value (2.0–3.0 W/mK) of yttria stabilized zirconia. The ultralow thermal conductivity in the studied CuSCN phases are attributed to the avoided crossing between the LA phonons and low-lying optical branches, the weak chemical bonding and strong anharmonicity. The calculated *ZT* values of α- and β-CuSCN are 1.7 and 2.1 at 800 K, respectively, which are comparable to that of some well-known thermoelectric materials. Furthermore, both α- and β-CuSCN phases are found to exhibit large negative thermal expansion coefficients induced by the transverse vibrations of carbon and nitrogen atoms. These findings suggest that CuSCN is promising for thermal management as well as for thermoelectric device, thus expanding the applications of CuSCN from solar cells to thermal devices.

Declaration of competing interest

The authors declare that they have no known competing financial interests or personal relationships that could have appeared to influence the work reported in this paper.

CRediT authorship contribution statement

Yupeng Shen: Conceptualization, Writing - original draft, Methodology, Software, Formal analysis, Investigation, Data curation, Visualization. **Fancy Qian Wang:** Methodology, Software, Formal analysis, Investigation, Data curation, Visualization. **Qian Wang:** Conceptualization, Funding acquisition, Project administration, Software, Writing - review & editing, Validation, Resources, Supervision.

Acknowledgments

This work is partially supported by grants from the National Natural Science Foundation of China (Grants No. NSFC-11974028 and NSFC-21773004), and the National Key Research and Development Program of the Ministry of Science and Technology of China (Grants No. 2016YFE0127300 and 2017YFA0205003), and is supported by the High-Performance Computing Platform of Peking University, China.

Appendix A. Supplementary data

Supplementary data to this article can be found online at https://doi.org/10.1016/j.nanoen.2020.104822.

References

[1] E.S. Toberer, A. Zevalkink, G.J. Snyder, Phonon engineering through crystal chemistry, J. Mater. Chem. 21 (40) (2011) 15843–15852.
[2] P. Klemens, M. Gell, Thermal conductivity of thermal barrier coatings, Mater. Sci. Eng., A 245 (2) (1998) 143–149.
[3] M.R. Winter, D.R. Clarke, Oxide materials with low thermal conductivity, J. Am. Ceram. Soc. 90 (2) (2007) 533–540.
[4] G. Lan, B. Ouyang, J. Song, The role of low-lying optical phonons in lattice thermal conductance of rare-earth pyrochlores: a first-principle study, Acta Mater. 91 (2015) 304–317.
[5] M. Watanabe, C. Mercer, C. Levi, A. Evans, A probe for the high temperature deformation of thermal barrier oxides, Acta Mater. 52 (6) (2004) 1479–1487.
[6] R. Vaßen, M.O. Jarligo, T. Steinke, D.E. Mack, D. Stöver, Overview on advanced thermal barrier coatings, Surf. Coating. Technol. 205 (4) (2010) 938–942.
[7] A. Cipitria, I. Golosnoy, T. Clyne, A sintering model for plasma-sprayed zirconia TBCs. Part I: free-standing coatings, Acta Mater. 57 (4) (2009) 980–992.
[8] G.J. Snyder, E.S. Toberer, Complex Thermoelectric Materials, Materials for Sustainable Energy: a Collection of Peer-Reviewed Research and Review Articles from, Nature Publishing Group, World Scientific, 2011, pp. 101–110.
[9] L.-D. Zhao, S.-H. Lo, Y. Zhang, H. Sun, G. Tan, C. Uher, et al., Ultralow thermal conductivity and high thermoelectric figure of merit in SnSe crystals, Nature 508 (7496) (2014) 373.
[10] C.W. Li, J. Hong, A.F. May, D. Bansal, S. Chi, T. Hong, et al., Orbitally driven giant phonon anharmonicity in SnSe, Nat. Phys. 11 (12) (2015) 1063.
[11] Z. Gao, F. Tao, J. Ren, Unusually low thermal conductivity of atomically thin 2D tellurium, Nanoscale 10 (27) (2018) 12997–13003.
[12] K. Tennakone, G.S. Pushpa, S. Punchihewa, G. Epa, Stability of cuprous thiocyanate coated cuprous oxide photocathode in aqueous thiocyanate, Electrochim. Acta 31 (3) (1986) 315–318.
[13] P. Pattanasattayavong, V. Promarak, T.D. Anthopoulos, Electronic properties of copper (I) thiocyanate (CuSCN), Adv. Electron. Mater. 3 (3) (2017) 1600378.
[14] D. Smith, V. Saunders, The structure and polytypism of the β modification of copper (I) thiocyanate, Acta Crystallogr. B 37 (10) (1981) 1807–1812.
[15] N. Arora, M.I. Dar, A. Hinderhofer, N. Pellet, F. Schreiber, S.M. Zakeeruddin, et al., Perovskite solar cells with CuSCN hole extraction layers yield stabilized efficiencies greater than 20%, Science 358 (6364) (2017) 768–771.
[16] P. Pattanasattayavong, N. Yaacobi-Gross, K. Zhao, G.O.N. Ndjawa, J. Li, F. Yan, et al., Hole-transporting transistors and circuits based on the transparent inorganic semiconductor copper (I) thiocyanate (CuSCN) processed from solution at room temperature, Adv. Mater. 25 (10) (2013) 1504–1509.
[17] A. Perumal, H. Faber, N. Yaacobi-Gross, P. Pattanasattayavong, C. Burgess, S. Jha, et al., High-Efficiency, Solution-Processed, Multilayer phosphorescent organic light-emitting diodes with a copper thiocyanate hole-injection/hole-transport layer, Adv. Mater. 27 (1) (2015) 93–100.
[18] E. Premalal, N. Dematage, G. Kumara, R. Rajapakse, M. Shimomura, K. Murakami, et al., Preparation of structurally modified, conductivity enhanced-p-CuSCN and its application in dye-sensitized solid-state solar cells, J. Power Sources 203 (2012) 288–296.
[19] N. Yaacobi-Gross, N.D. Treat, P. Pattanasattayavong, H. Faber, A.K. Perumal, N. Stingelin, et al., High-efficiency organic photovoltaic cells based on the solution-processable hole transporting interlayer copper thiocyanate (CuSCN) as a replacement for PEDOT: PSS, Adv. Energy Mater. 5 (3) (2015) 1401529.
[20] P.E. Blöchl, Projector augmented-wave method, Phys. Rev. B 50 (24) (1994) 17953–17979.
[21] G. Kresse, J. Furthmüller, Efficient iterative schemes for ab initio total-energy calculations using a plane-wave basis set, Phys. Rev. B 54 (16) (1996) 11169.
[22] J.P. Perdew, K. Burke, M. Ernzerhof, Generalized gradient approximation made simple, Phys. Rev. Lett. 77 (18) (1996) 3865.
[23] W. Li, J. Carrete, N.A. Katcho, N. Mingo, ShengBTE, A solver of the Boltzmann transport equation for phonons, Comput. Phys. Commun. 185 (6) (2014) 1747–1758.
[24] L.-F. Huang, X.-Z. Lu, E. Tennessen, J.M. Rondinelli, An efficient ab-initio quasiharmonic approach for the thermodynamics of solids, Comput. Mater. Sci. 120 (2016) 84–93.
[25] L.-F. Huang, N.Z. Koocher, M. Gu, J.M. Rondinelli, Structure dependent phase stability and thermal expansion of ruddlesden–popper strontium titanates, Chem. Mater. 30 (20) (2018) 7100–7110.
[26] L.-F. Huang, X.-Z. Lu, J.M. Rondinelli, Tunable negative thermal expansion in layered perovskites from quasi-two-dimensional vibrations, Phys. Rev. Lett. 117 (11) (2016) 115901.
[27] S. Baroni, P. Giannozzi, E. Isaev, Density-functional perturbation theory for quasi-harmonic calculations, Rev. Mineral. Geochem. 71 (1) (2010) 39–57.
[28] A. Togo, L. Chaput, I. Tanaka, G. Hug, First-principles phonon calculations of thermal expansion in Ti_3SiC_2, Ti_3AlC_2, and Ti_3GeC_2, Phys. Rev. B 81 (17) (2010) 174301.
[29] A. Togo, I. Tanaka, First principles phonon calculations in materials science, Scripta Mater. 108 (2015) 1–5.
[30] W. Ji, G.-Q. Yue, F.-S. Ke, S. Wu, H.-B. Zhao, L.-Y. Chen, et al., Electronic structures and optical properties of CuSCN with Cu vacancies, J. Kor. Phys. Soc. 60 (8) (2012) 1253–1257.
[31] L. Tsetseris, Two-dimensional copper thio-and seleno-cyanates, Phys. Chem. Chem. Phys. 18 (11) (2016) 7837–7840.
[32] M. Kabešová, M. Dunaj-Jurčo, M. Serator, J. Gažo, J. Garaj, The crystal structure of copper (I) thiocyanate and its relation to the crystal structure of copper (II) diammine dithiocyanate complex, Inorg. Chim. Acta. 17 (1976) 161–165.

[33] O. Delaire, J. Ma, K. Marty, A.F. May, M.A. McGuire, M.-H. Du, et al., Giant anharmonic phonon scattering in PbTe, Nat. Mater. 10 (8) (2011) 614.
[34] M. Christensen, A.B. Abrahamsen, N.B. Christensen, F. Juranyi, N.H. Andersen, K. Lefmann, et al., Avoided crossing of rattler modes in thermoelectric materials, Nat. Mater. 7 (10) (2008) 811.
[35] W. Li, J. Carrete, G.K. Madsen, N. Mingo, Influence of the optical-acoustic phonon hybridization on phonon scattering and thermal conductivity, Phys. Rev. B 93 (20) (2016) 205203.
[36] T. Tadano, Y. Gohda, S. Tsuneyuki, Impact of rattlers on thermal conductivity of a thermoelectric clathrate: a first-principles study, Phys. Rev. Lett. 114 (9) (2015), 095501.
[37] R.L. González-Romero, A. Antonelli, A.S. Chaves, J.J. Meléndez, Ultralow and anisotropic thermal conductivity in semiconductor As_2Se_3, Phys. Chem. Chem. Phys. 20 (3) (2018) 1809–1816.
[38] P. Norouzzadeh, C.W. Myles, D. Vashaee, Phonon dynamics in type-VIII silicon clathrates: beyond the rattler concept, Phys. Rev. B 95 (19) (2017) 195206.
[39] S. Zhang, R. Zhang, AELAS: automatic ELAStic property derivations via high-throughput first-principles computation, Comput. Phys. Commun. 220 (2017) 403–416.
[40] D. Yang, W. Yao, Y. Yan, W. Qiu, L. Guo, X. Lu, C. Uher, X. Han, G. Wang, T. Yang, Intrinsically low thermal conductivity from a quasi-one-dimensional crystal structure and enhanced electrical conductivity network via Pb doping in $SbCrSe_3$, NPG Asia Mater. 9 (6) (2017) e387.
[41] L.-D. Zhao, J. He, D. Berardan, Y. Lin, J.-F. Li, C.-W. Nan, N. Dragoe, BiCuSeO oxyselenides: new promising thermoelectric materials, Energy Environ. Sci. 7 (9) (2014) 2900–2924.
[42] Y. Xiao, C. Chang, Y. Pei, D. Wu, K. Peng, X. Zhou, S. Gong, J. He, Y. Zhang, Z. Zeng, Origin of low thermal conductivity in SnSe, Phys. Rev. B 94 (12) (2016) 125203.
[43] L. Xu, Y. Zheng, J.-C. Zheng, Thermoelectric transport properties of PbTe under pressure, Phys. Rev. B 82 (19) (2010) 195102.
[44] L.-D. Zhao, S.-H. Lo, Y. Zhang, H. Sun, G. Tan, C. Uher, C. Wolverton, V.P. Dravid, M.G. Kanatzidis, Ultralow thermal conductivity and high thermoelectric figure of merit in SnSe crystals, Nature 508 (7496) (2014) 373–377.
[45] H. Wang, E. Schechtel, Y. Pei, G.J. Snyder, High thermoelectric efficiency of n-type PbS, Adv. Energy Mater. 3 (4) (2013) 488–495.
[46] F.Q. Wang, M. Hu, Q. Wang, Ultrahigh thermal conductivity of carbon allotropes with correlations with the scaled Pugh ratio, J. Mater. Chem. 7 (11) (2019) 6259–6266.
[47] C. Toher, J.J. Plata, O. Levy, M. De Jong, M. Asta, M.B. Nardelli, S. Curtarolo, High-throughput computational screening of thermal conductivity, Debye temperature, and Grüneisen parameter using a quasiharmonic Debye model, Phys. Rev. B 90 (17) (2014) 174107.
[48] M.K. Jana, K. Pal, A. Warankar, P. Mandal, U.V. Waghmare, K. Biswas, Intrinsic rattler-induced low thermal conductivity in Zintl type $TlInTe_2$, J. Am. Chem. Soc. 139 (12) (2017) 4350–4353.
[49] Z. Feng, T. Jia, J. Zhang, Y. Wang, Y. Zhang, Dual effects of lone-pair electrons and rattling atoms in CuBiS 2 on its ultralow thermal conductivity, Phys. Rev. B 96 (23) (2017) 235205.
[50] A. Fischer, E.-W. Scheidt, W. Scherer, D. Benson, Y. Wu, D. Eklöf, U. Häussermann, Thermal and vibrational properties of thermoelectric ZnSb: exploring the origin of low thermal conductivity, Phys. Rev. B 91 (22) (2015) 224309.
[51] G.K.H. Madsen, J. Carrete, M.J. Verstraete, BoltzTraP2 , a program for interpolating band structures and calculating semi-classical transport coefficients, Comput. Phys. Commun. 231 (2018) 140–145.
[52] K. Pal, Y. Xia, J. He, C. Wolverton, High thermoelectric performance in $BaAgYTe_3$ via low lattice thermal conductivity induced by bonding heterogeneity, Phys. Rev. Mater. 3 (8) (2019), 085402.
[53] F.Q. Wang, S. Zhang, J. Yu, Q. Wang, Thermoelectric properties of single-layered SnSe sheet, Nanoscale 7 (38) (2015) 15962–15970.
[54] X. Yang, X. Cheng, X. Yan, J. Yang, T. Fu, J. Qiu, Synthesis of ZrO_2/ZrW_2O_8 composites with low thermal expansion, Compos. Sci. Technol. 67 (6) (2007) 1167–1171.
[55] T. Mary, J. Evans, T. Vogt, A. Sleight, Negative thermal expansion from 0.3 to 1050 Kelvin in ZrW2O8, Science 272 (5258) (1996) 90–92.
[56] B.K. Greve, K.L. Martin, P.L. Lee, P.J. Chupas, K.W. Chapman, A.P. Wilkinson, Pronounced negative thermal expansion from a simple structure: cubic ScF_3, J. Am. Chem. Soc. 132 (44) (2010) 15496–15498.
[57] D.A. Woodcock, P. Lightfoot, L.A. Villaescusa, M.-J. Díaz-Cabañas, M.A. Camblor, D. Engberg, Negative thermal expansion in the siliceous zeolites chabazite and ITQ-4: a neutron powder diffraction study, Chem. Mater. 11 (9) (1999) 2508–2514.
[58] J. Tao, A. Sleight, The role of rigid unit modes in negative thermal expansion, J. Solid State Chem. 173 (2) (2003) 442–448.
[59] Z. Liu, Q. Gao, J. Chen, J. Deng, K. Lin, X. Xing, Negative thermal expansion in molecular materials, Chem. Commun. 54 (41) (2018) 5164–5176.